# Geostrophic and Mesoscale Eddy Contributions to the Atlantic Meridional Overturning Circulation Decline Under CO2 Increase in the GFDL CM2-O Model Suite

Anne-Sophie Fortin, Carolina O Dufour, Timothy Merlis, Rym Msadek

# Geostrophic and Mesoscale Eddy Contributions to the Atlantic Meridional Overturning Circulation Decline Under $CO_2$ Increase in the GFDL CM2-O Model Suite

Anne-Sophie Fortin, [a] Carolina O. Dufour, [a] Timothy M. Merlis, [b] Rym Msadek, [c]

[a] *Department of Atmospheric and Oceanic Sciences, McGill University, Montreal, Quebec, Canada*

[b] *Program in Atmospheric and Oceanic Sciences, Princeton University, Princeton, NJ, USA*

[c] *CECI, Université de Toulouse, CNRS, CERFACS, Toulouse, France*

*Corresponding author*: Anne-Sophie Fortin, anne-sophie.fortin@mail.mcgill.ca



**Early Online Release**: This preliminary version has been accepted for publication in *Journal of Climate*, may be fully cited, and has been assigned DOI 10.1175/JCLI-D-22-0561.1. The final typeset copyedited article will replace the EOR at the above DOI when it is published.

ABSTRACT: The pattern and magnitude of the Atlantic Meridional Overturning Circulation (AMOC) in response to an increase in atmospheric carbon dioxide ($CO_2$) concentration greatly differ across climate models in particular due to differences in the representation of oceanic processes. Here, we investigate the response of the AMOC to an idealized climate change scenario, along with the drivers of this response, in the three configurations of a coupled climate model suite with varying resolutions in the ocean (1°, 0.25°, 0.10°). In response to the $CO_2$ increase, the AMOC shows a reduction of similar magnitude in the low and high resolutions, while a muted response is found in the medium resolution. A decomposition of the AMOC into its geostrophic and residual components reveals that most of the AMOC reduction is due to a weakening of the geostrophic streamfunction driven by temperature anomalies, partly opposed by a strengthening of the geostrophic streamfunction driven by salinity anomalies. Changes in the AMOC due to the mesoscale eddy streamfunction contribute to 13% and 17% of the AMOC decline in the low and high resolutions, respectively, but induce very little change in the medium resolution. The similar response of the AMOC strength in the low and high resolutions hides important differences in the contribution and pattern of the geostrophic and eddy streamfunctions. The lack of sensitivity of the medium resolution to the $CO_2$ forcing is due to a weak connection between the deep-water formation regions in the northern subpolar gyre and the Deep Western Boundary Current.





Accepted for publication in *Journal of Climate*. DOI 10.1175/JCLI-D-22-0561.1.

SIGNIFICANCE STATEMENT: The Atlantic Meridional Overturning Circulation (AMOC) is a major system of ocean currents in the Atlantic that contributes to shaping the climate at regional and global scales, notably through the transport of heat from the low to the high latitudes. A major slowdown of the AMOC over the 21st century is predicted by current climate models in response to increasing greenhouse gases. Yet, the magnitude and timing of this slowdown are uncertain. The purpose of this study is to investigate the expected weakening of the AMOC using state-of-the-art numerical climate models that include higher resolutions than typically used in climate change assessments. Our results provide insights into the mechanisms driving the weakening of the AMOC and into differences arising from model resolutions.





Accepted for publication in *Journal of Climate*. DOI 10.1175/JCLI-D-22-0561.1.

## 1. Introduction

The Atlantic Meridional Overturning Circulation (AMOC), which refers to the net northward flow of warm water in the Atlantic surface compensated by a southward flow at depth, redistributes about 1 PW ($10^{15}$ W) of heat northward (Hartmann 2015). The AMOC is fed by the formation of dense water masses at the surface in the North Atlantic that are transported southward in the deep ocean (Buckley and Marshall 2016; Johnson et al. 2019). This formation of dense waters contributes to the ventilation of the deep ocean (Read 2000) and to the sequestration of the anthropogenic carbon and excess heat taken up at the surface (Rhein et al. 2013). Thus, changes in the AMOC have important implications for regional and global climate (Zhang et al. 2019; Jackson et al. 2015).

Since 2004, direct observations of the ocean circulation have been obtained by the Rapid Climate Change-Meridional Overturning Circulation and Heatflux Array (RAPID-MOCHA) at 26.5°N (hereinafter referred to as the RAPID array; McCarthy et al. 2012; Moat et al. 2020a). The AMOC in the North Atlantic has also been monitored since 2014 by the Overturning in the Subpolar North Atlantic Program (OSNAP) observing system which has two arrays, one deployed between the southern Labrador shelf and the southwestern tip of Greenland, and the other deployed between the southeastern tip of Greenland and Scotland (Lozier et al. 2017). The short observational period and large temporal variability for all observed timescales (Smeed et al. 2015; Lozier et al. 2019) have so far made detecting a secular trend challenging (Lobelle et al. 2020). Indeed, while the RAPID observations over the 2004–2012 period suggested a significant weakening of the AMOC (Smeed et al. 2014), a recovery of the AMOC has been observed following the record minimum reached in 2010 (Roberts et al. 2014; Parker and Ollier 2016; Smeed et al. 2018; Moat et al. 2020b).

The main physical mechanisms at play in the AMOC variability vary with the timescale of interest. On weekly to inter-annual timescales, AMOC variability can be predicted by wind-driven processes, i.e., Ekman transport, upon which the chaotic variability from mesoscale eddies and internal waves is added (Buckley and Marshall 2016; Hirschi et al. 2020). At centennial timescale, AMOC variability can be accounted for by geostrophic flows (Buckley and Marshall 2016; Waldman et al. 2020). The geostrophic component of the AMOC is greatly affected by the formation and southward propagation of dense waters from deep convection sites in the northern part of the basin. Which convection site contributes most to the AMOC variability is however





Accepted for publication in *Journal of Climate*. DOI 10.1175/JCLI-D-22-0561.1.

under debate. Some preliminary results from 21 months of OSNAP observations suggest that most of the AMOC variability on monthly timescales comes from the Norwegian Sea rather than from the Labrador Sea (Lozier et al. 2019) contrasting with what many modelling studies had suggested (Eden and Willebrand 2001; Bailey et al. 2005; Getzlaff et al. 2005; Danabasoglu et al. 2012). The AMOC variability at decadal timescales is due to a combination of processes at both inter-annual and centennial timescales, which are not well understood as the observational record is too short. As the AMOC is nearly geostrophically balanced on inter-annual to decadal time scales and the Ekman component of the AMOC only dominates at shorter time scales, the wind-driven response of the AMOC to climate change is often ignored when investigating the AMOC response to anthropogenic forcings (Buckley and Marshall 2016; Levang and Schmitt 2020; Waldman et al. 2020) and will not be investigated in this study. Rather, we will focus on the geostrophic flows and mesoscale eddies' response to anthropogenic forcing at decadal timescales.

The overwhelming majority of models that participate in the Coupled Model Intercomparison Project Phase 5 (CMIP5) and phase 6 (CMIP6) predict a slowdown of the AMOC for the next century regardless of the anthropogenic forcing scenario used (Collins et al. 2013; Weijer et al. 2020). The magnitude of the change in the AMOC is uncertain though, with this uncertainty projecting on other major global changes such as the surface temperature response and wind patterns (Bellomo et al. 2021). Constraining the relationship between the AMOC strength and its decline in CMIP6 models with RAPID estimates suggests that the AMOC will decline by 34% by 2100 under an aggressive mitigation scenario and by 45% under a business-as-usual scenario, which corresponds to a decrease of about 6 to 8 Sv (Weijer et al. 2020). While the possibility of an abrupt collapse by 2100 remains unlikely according to the most recent report of the Intergovernmental Panel on Climate Change (Fox-Kemper et al. 2021), a rapid transition of the AMOC to a weaker mode is suggested by the observations (Boers 2021).

Many studies attribute the AMOC weakening to a decrease in density of the North Atlantic surface waters due to their warming and freshening from increased air temperature, ice melting, and precipitation over this region, thus reducing deep water formation (Buckley and Marshall 2016). A significant decline is found in response to the melting of Arctic sea ice or Greenland ice sheet in many models (e.g. Weijer et al. 2012; Jackson 2013; Jackson and Wood 2018; Haskins et al. 2019). Warm and fresh anomalies propagate deep into the water column as a result of convective




Accepted for publication in *Journal of Climate*. DOI 10.1175/JCLI-D-22-0561.1.

events in the North Atlantic. Jansen and Nadeau (2019) show that the AMOC decline is not only due to changes in density at the surface but also to a reduction of the meridional subsurface density gradient as North Atlantic Deep Water (NADW) warms. This reduction in the subsurface density gradient decreases the poleward transport, and thus slows down the AMOC. However, Levang and Schmitt (2020) find a more nuanced relationship between the subpolar gyre buoyancy and the AMOC strength as their results suggest that subtropical waters anomalies are transported at intermediate depth and have an important impact on the geostrophic transport.

Arising from the time-dependent chaotic component of the circulation, mesoscale eddies have also been shown to significantly impact the AMOC. Through the advection of heat and salt in deep convection regions, mesoscale and submesoscale eddies influence the formation of dense waters, which in turn impacts the AMOC strength and variability (e.g., Tagklis et al. 2020). A lack of representation of mesoscale and submesoscale eddies has been linked to an overproduction of Labrador Sea Water in models due to insufficient restratification of the water column after convective events. This overproduction has been identified as a possible cause for the predominance of the Labrador Sea in the AMOC variability in models (Li et al. 2019). Indeed, a common bias found among relatively coarse resolution models at high latitudes is too extensive and deep mixed layers (Talandier 2015; Rieck et al. 2019). Finally, once deep waters are formed, mesoscale eddies contribute to their propagation to lower latitudes along an interior pathway (Lozier 1997; Bower et al. 2009).

Previous studies have looked at the role of mesoscale eddies on the AMOC strength through increasing horizontal resolution in ocean models. Using a regional ocean model driven by atmospheric reanalysis, Talandier et al. (2014) showed that increasing resolution from 0.5° to 0.125° improves the representation of the Western North Atlantic current system and strengthens the AMOC. Hirschi et al. (2020) looked at the difference in AMOC mean state between ocean models ranging from 1° to 0.08° and found that higher resolution models generally provide a better representation of the AMOC pathways and variability at observed time scales. Winton et al. (2014) and Jackson et al. (2020) both found that the mean state of the AMOC depends on whether mesoscale eddies are explicitly resolved or parameterized; this mean state, in turn, sets the magnitude of the response to $CO_2$ increase. More specifically, Jackson et al. (2020) compared two climate models at 1° and 0.25° in the ocean and noted both a stronger AMOC and a larger reduction in the AMOC





Accepted for publication in *Journal of Climate*. DOI 10.1175/JCLI-D-22-0561.1.

in the 0.25° model under a climate change scenario. However, the size of the ensembles was quite small, which could affect the conclusion or robustness of the results.

Quantifying the contribution of resolved mesoscale eddies to the decline of the AMOC has not been thoroughly examined to date. Few studies have investigated the AMOC response to $CO_2$ increase using climate models with resolution ranging from non-eddying to eddying in the ocean (e.g., Jackson et al. 2020). However, these studies have not attempted to decompose the drivers of the response, including the contribution from eddies. Furthermore, the computational cost of running eddy-rich ocean components in climate models over time periods meaningful for climate has impeded such attempts.

In this paper, we use a coupled climate model suite, which has three ocean configurations with horizontal resolutions of 1°, 0.25°, and 0.1°, with each configuration run under preindustrial conditions and under an idealized climate change scenario. This model suite allows us to investigate the respective contributions of time-mean and eddy-induced transports to the response of the AMOC to climate change across a broad range of resolutions spanning from non-eddying to eddy-rich. The rest of the paper is organized as follows. Section 2 describes the climate model suite and the decomposition of AMOC components. Section 3 presents the response of the AMOC to climate change and the respective contributions of the eddy and time-mean components to this response. Section 4 discusses the singularity of our medium-resolution configuration and the causes of the density anomalies that drive the geostrophic AMOC decline. Section 5 summarizes the results.

## 2. Methods

### *a. Models and Simulations*

#### 1) The CM2-O Suite

We use the Climate Model version 2.0-Ocean (CM2-O suite) developed by the Geophysical Fluid Dynamics Laboratory (GFDL). The CM2-O suite is a hierarchy of three fully coupled climate models (CM2-1deg, CM2.5, and CM2.6) run at varying horizontal resolutions in the ocean (1°, 0.25°, and 0.1°, respectively). The atmosphere and land configurations are the same across the CM2-O suite. The atmospheric resolution is roughly 50 km (Delworth et al. 2012). The resolution of the sea ice model is the same as the ocean and thus differs across the CM2-O suite. The ocean component uses the Modular Ocean Model, version 5 (MOM5; Griffies et al. 2015). The ocean's




Accepted for publication in *Journal of Climate*. DOI 10.1175/JCLI-D-22-0561.1.

vertical grid has 50 levels and extends to 5500 meters deep, with a finer resolution at the surface (10 meters) and coarser resolution at depth (210 meters). As these models share the same code but are configured differently through the use of different horizontal resolutions and parameterizations we refer to them as model configurations, or simply configurations. Additionally, the different model configurations will be referred hereafter to as the low-resolution (LR), medium-resolution (MR), and high-resolution (HR).

The parameterization representing the effect of mesoscale eddies on the circulation in the LR is implemented using Ferrari et al. (2010) formulation, adapted from Gent et al. (1995) parameterization (hereafter referred to as *GM* for simplicity). Mesoscale eddies equatorward of approximately 30° and 50° are resolved in the MR and HR respectively (Griffies et al. 2015; Hallberg 2013). No mesoscale eddy parameterization has been used for those two model configurations because having such parameterizations suppresses the growth of resolved eddies. All model configurations of the CM2-O suite have a sub-mesoscale eddy parameterization to represent the restratification by mixed layer submesoscale eddies following Fox-Kemper et al. (2011). For a more complete description of the CM2-O suite, the reader is referred to Delworth et al. (2012) for detailed documentation of CM2.5 and CM2.6 configurations, to Decuypère et al. (2022) for an investigation of the impact of ocean heat transport on Arctic sea ice, and to Griffies et al. (2015) for an investigation of the role of mesoscale eddies on the models' drift and heat budget in the three model configurations.

Finally, no tuning of the configurations was done. In sum, the CM2-O suite is a hierarchy of three model configurations allowing us to investigate the impacts of refining horizontal resolution in the ocean on various aspects of the climate.

### 2) Simulations

Each configuration of the CM2-O suite is run under a control and an idealized climate change scenario, allowing for an analysis of the AMOC response to climate change. The *control* runs are integrated for 200 years from the World Ocean Atlas 2018 (WOA; Locarnini et al. 2018) with a prescribed pre-industrial carbon dioxide ($CO_2$) level kept constant at 286 ppm. The *climate change* run is branched off the control run at year 121 and is integrated for 80 years under 1% per year increasing $CO_2$ levels. So, both our control and climate change runs end at year 200. Unless otherwise specified, we consider the last 20 years when presenting time averages. Important




Accepted for publication in *Journal of Climate*. DOI 10.1175/JCLI-D-22-0561.1.

circulation features, such as the upper cell of the AMOC (see Fig. 4) and the Antarctic Circumpolar Current (see Fig. 1a of Dufour et al. 2015), and global sea surface temperature (SST; not shown) reach a near steady-state after 100 years. This equilibration time is similar to what Griffies et al. (2015) showed for the same CM2-O suite run with a constant radiative forcing with the same initialization strategy (see their figure 2). The small model drift that remains does not affect our analysis because we use the differences between two simulations that share the same drift by construction. When showing diagnostics of the individual runs instead of the difference, we remove the drift beforehand and indicate it in the caption of the figure.

### *b. Decomposition of the AMOC*

The AMOC is defined as the meridional-depth overturning streamfunction ($\Psi$) in the Atlantic Ocean with units of Sverdrup (1 Sv = $10^9$ kg/s). The *upper cell* of the AMOC ($\Psi > 0$) consists of a northward-flowing upper limb and a southward-flowing lower limb down to about 4 km. Underneath, the *lower cell* of the AMOC ($\Psi < 0$) consists of a southward-flowing upper limb and a northward-flowing lower limb fed by the dense Antarctic Bottom Water.

#### 1) Eddy and time mean components

To investigate the contributions of the time-mean and eddy streamfunctions to the AMOC and their respective responses to climate change, we use a density framework which avoids spurious circulation features arising from zonally averaging in depth space and reveals the contribution of mesoscale eddies to the total streamfunction (Gent et al. 1995; McIntosh and McDougall 1996). At a given time, the total AMOC ($\Psi$) can be written as:

$$\Psi(y, \sigma_2) = \int dx \int_{-H}^{z(x,y,\sigma_2)} V(x, y, z')\rho_0 dz', \tag{1}$$

where $V$ is the meridional velocity, $\sigma_2$ is the potential density referenced to 2 km, $H$ is the spatially varying ocean bottom depth, $z$ is the depth of the $\sigma_2$ isopycnal, and $\rho_0$ is the constant Boussinesq reference density (set to 1035 kg m$^{-3}$). The total AMOC can be defined in a similar way in depth space (no binning required) and is discussed in several places in the manuscript for comparison with previous work.




Accepted for publication in *Journal of Climate*. DOI 10.1175/JCLI-D-22-0561.1.

The total AMOC from equation 1 can be decomposed as follows:

$$\Psi = \bar{\Psi} + \Psi^*, \tag{2}$$

where $\bar{\Psi}$ is the Eulerian-mean streamfunction (resulting from the time-mean flow) and $\Psi^*$ is the mesoscale eddy-induced streamfunction (resulting from the temporal anomalies relative to the time-mean flow). The mesoscale eddy-induced streamfunction corresponds to the component explicitly resolved by the model ($\Psi^*_{res}$) plus, for the LR configuration, the component arising from the parameterized mesoscale eddy streamfunction using the GM parameterization ($\Psi^*_{GM}$):

$$\Psi^* = \Psi^*_{res} + \Psi^*_{GM}. \tag{3}$$

For model configurations without mesoscale eddy parameterization, such as the MR and HR, $\Psi^* = \Psi^*_{res}$.

The resolved component of the overturning streamfunction ($\Psi_{res} = \bar{\Psi} + \Psi^*_{res}$) is obtained from the meridional transport computed at each time step in the model and binned in density coordinates. $\bar{\Psi}$ is computed and binned in density coordinates offline from the 20-year monthly climatology of velocity and density fields. The resolved-eddy component $\Psi*_{res}$ is obtained by subtracting $\bar{\Psi}$ from $\Psi_{res}$. Finally, $\Psi^*_{GM}$ is calculated as follows:

$$\Psi^*_{GM}(y, \sigma_2) = \int \rho_0 \kappa S_y(y, \sigma_2) dx \tag{4}$$

Where $\kappa$ is the kinematic diffusivity (>0) and $S_y$ is the neutral slope in the y-direction. The integrand is calculated online and binned in density coordinates at each time step in the LR configuration where the mesoscale eddy parameterization is used.

The contribution of the submesoscale eddy parameterization to the AMOC is not accounted for because the outputs necessary to the calculation have not been saved for all model configurations over the whole time period of interest. An estimate of that contribution over the last 20 years of the control simulation shows that, in the MR and HR configurations, this term is negligible, while in the LR configuration, it ranges between 1 and 3 Sv, and is localized mostly at the surface and down to 2 km around 60°N where deep convection occurs (not shown). The larger sub-mesoscale




Accepted for publication in *Journal of Climate*. DOI 10.1175/JCLI-D-22-0561.1.

parameterized contribution in the LR compared to the MR and HR can be explained by the deeper and wider area of convection over which the parameterization operates (Fig. 1j-l). This difference is likely caused by the weak re-stratification of the water column in the LR due to the lack of resolved eddies.

2) Geostrophic component

To investigate the role of temperature and salinity anomalies in the response of $\bar{\Psi}$ to climate change, we calculate the geostrophic AMOC streamfunction ($\Psi_{geo}$) using the thermal wind relation in depth space. We first compute the geostrophic velocity ($\overline{V_g}$) from the density at the westernmost ($\rho_w$) and easternmost ($\rho_e$) grid points, following the topography along the continental slopes.

$$\overline{V_g}(z) = \frac{g}{\rho_0 f} \int_{-H}^{z} \frac{1}{L(z)} (\rho_w - \rho_e) dz', \tag{5}$$

where g is the gravitational acceleration, $f$ is the Coriolis parameter, H is the ocean depth, $L(z)$ is the width of the basin, and the suffixes $w$ and $e$ refer to west and east, respectively. Then, the overturning streamfunction ($\Psi_{geo}$) is computed following Levang and Schmitt (2020).

$$\Psi_{geo}(z) = L(z)\rho_0 \int_{-H}^{z} \left( \overline{V_g} - \frac{1}{H} \int_{-H}^{\eta} \overline{V_g} dz' \right) dz', \tag{6}$$

where $\eta$ is the free surface height. The vertically averaged geostrophic velocity, the right term in the integrand in equation (6), is subtracted to ensure mass conservation.

The geostrophic AMOC streamfunction is a good approximation of the Eulerian-mean streamfunction on the time scale investigated (e.g. Levang and Schmitt 2020; Waldman et al. 2020). For all model configurations across the suite, the geostrophic AMOC streamfunction remains very close to the Eulerian-mean streamfunction in the upper cell (within 2 to 3 Sv; not shown), but not in the lower cell where the southward circulation below 3 km is not well-represented in the geostrophic AMOC.




Accepted for publication in *Journal of Climate*. DOI 10.1175/JCLI-D-22-0561.1.

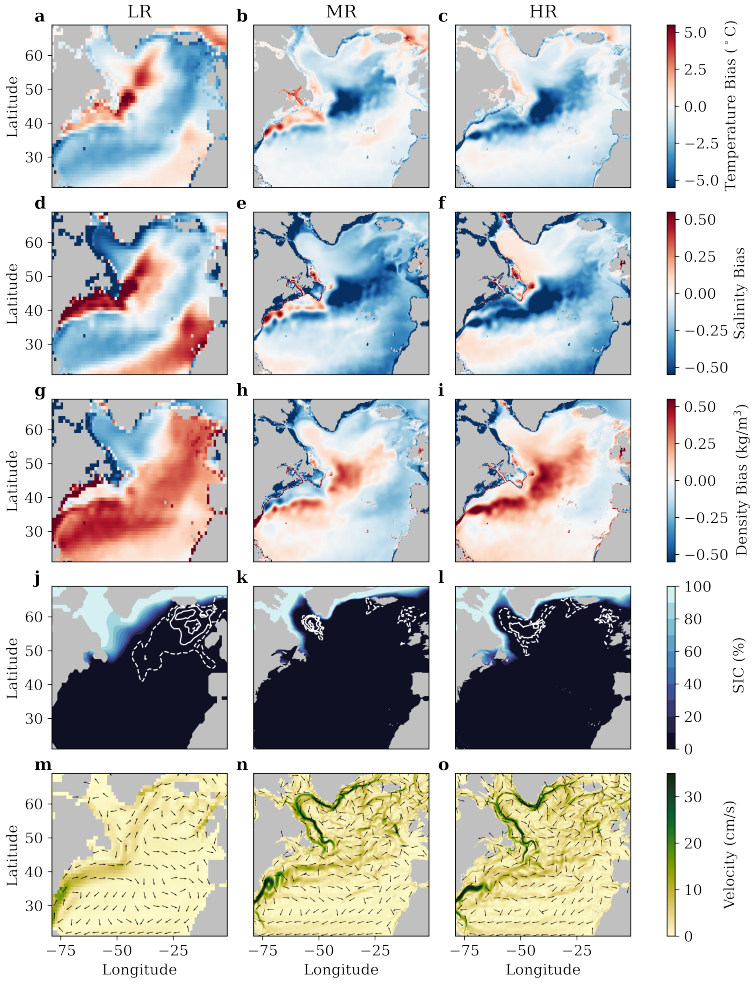


FIG. 1. Biases across the CM2-O suite in (a-c) potential temperature, (d-f) salinity, and (g-i) potential density referenced to the surface ($\sigma_0$) upper ocean (0-730 m). The upper ocean properties biases have been computed as the difference between the model outputs over the years 147 to 156 of the climate change scenario and the World Ocean Atlas climatology from 2005 to 2017 (downloaded at https://accession.nodc.noaa.gov/NCEI-WOA18 on July 2021), where the $CO_2$ concentration and the time period length are similar for both products. (j-l) Sea ice concentration overlaid with the winter (JFM) mixed layer depth (white contours with thin dotted lines corresponding to 500 meters, and solid lines to 1000, 2000, and 3000 meters). (m-o) CM2-O suite absolute horizontal velocities averaged over 0-730 m (colors) and their direction (arrows). All model outputs are averaged over the years 147-156 of the climate change simulations.





Accepted for publication in *Journal of Climate*. DOI 10.1175/JCLI-D-22-0561.1.

*c. Model Evaluation and preindustrial control state*

1) Upper Ocean Properties

We present the upper ocean (0-730 m) model biases in temperature, salinity, and density, along with model winter mixed layer depth (MLD, used as a proxy for oceanic deep convection), sea-ice concentration (SIC), and absolute horizontal velocities in the North Atlantic in Figure 1. Here the biases are computed as the difference between the CM2-O suite over the years 147 to 156 of the climate change runs and modern-day observations from the World Ocean Atlas climatology, where the $CO_2$ concentration and the time period length are similar for both products. The MLD, SIC, and velocities are shown for the same time period.

The surface temperature bias generally dominates the density bias, except in the Labrador Sea. There, the LR configuration has a strong negative density bias due to a low salinity bias over the interior of the Labrador Sea. The poor representation of the Labrador Current over the continental slope in the LR configuration (Fig. 1m) results in the spreading of cold fresh waters from the Labrador Shelf to the interior of the Labrador Sea (Fig. 1d), similarly to what was described over the Antarctic continental slope in Lockwood et al. (2021). This freshwater anomaly strengthens the stratification thus leading to the suppression of convective activity over the Labrador Sea and an overly extensive sea-ice cover (Fig. 1j). The convection in the LR mostly occurs south of Iceland where an important positive density bias is found. In contrast, both the MR and HR configurations have a small positive density bias in the Labrador Sea and display convection in the central Labrador Sea, which extends over a larger area in the HR configuration (Fig. 1h-i, k-l). The location of convection is key for deep water formation as a water parcel convecting in the central Labrador Sea is more likely to be re-entrained while a water parcel convecting in the western boundary of the Labrador Sea is more likely to subduct and follow the Deep Western Boundary Current (DWBC; MacGilchrist et al. 2021).

In the center of the north Atlantic basin, the CM2-O suite exhibits a positive density bias due to a negative temperature bias. These biases, which are localized over the Gulf Stream and North Atlantic Current in MR and HR configurations and extend over a large portion of the Atlantic basin in the LR configuration, are associated with the representation of the Gulf Stream path and of the Nordic Sea overflows (Zhang et al. 2011; Danabasoglu et al. 2014; Griffies et al. 2015). Some improvement in the position of the Gulf Stream can be noticed at finer resolution with the Gulf





Accepted for publication in *Journal of Climate*. DOI 10.1175/JCLI-D-22-0561.1.

Stream separating at Cape Hatteras in the HR configuration as observed. In the LR configuration, in contrast, the Gulf Stream continues northward, hugging the coasts (Fig. 1m-o).

North of the Iceland-Faroe Ridge and the Faroe-Shetland Channel, there is a negative density bias due to warm and fresh biases for the three model configurations. South of the Iceland-Faroe Ridge and the Faroe-Shetland Channel, there is a positive density bias due to cold and fresh biases. This positive density bias is particularly strong in the LR configuration and its location corresponds to the area where most of its convective activity occurs. (Fig. 1g and j). Note that some convection also occurs in the MR and HR at the western tip of Iceland and near the Faroe-Shetland Channel.

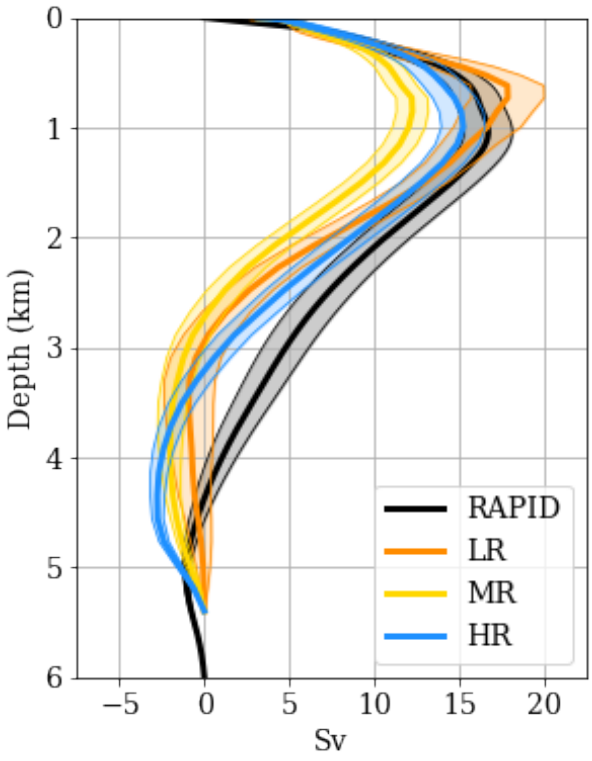


FIG. 2. AMOC at 26.5°N (in Sv) in the RAPID array estimate from 2004 to 2020 (black) and in the CM2-O suite over the years 181 to 200 inclusively. The shading indicates the ±1 standard deviation computed from yearly averages.

### 2) REPRESENTATION OF THE AMOC

We use the time-averaged RAPID array AMOC estimate from 2004 to 2020 (Frajka-Williams et al. 2021) to evaluate the representation of the AMOC at 26°N in the CM2-O suite. Note




Accepted for publication in *Journal of Climate*. DOI 10.1175/JCLI-D-22-0561.1.

that the following comparison should be taken with care as the AMOC observations used are not necessarily representative of an AMOC state that is compatible with that of the background radiative conditions in the preindustrial control experiments. Nonetheless, it allows us to situate the CM2-O suite control AMOC.

The LR configuration overestimates the upper cell of the AMOC while the MR and HR models underestimate it (Fig. 2). More precisely, the yearly-mean AMOC at RAPID has a maximum strength of 16.7 Sv ± 1.4 Sv while the LR, MR, and HR configurations have a maximum strength of 17.9 Sv ± 2.2 Sv, 12.3 Sv ± 0.9 Sv, and 15.3 Sv ± 1.3 Sv respectively. Thus, for all the model configurations but the MR, the maximum of the AMOC falls within 1 standard deviation of the observed maximum. The maximum strength is found at around 1 km in the RAPID estimate (1039 m) and in the HR (968 m), and at a shallower depth in the LR (665 m) and MR (781 m) configurations. The streamfunction goes to zero at a shallower depth in the models (2.9 km, 2.7 km, and 3.3 km for the LR, MR, and HR models, respectively) than in the RAPID estimate (4.4 km) meaning that the depth of the NADW is shallower in the CM2-O suite than in the observations. This is also observed for the ensemble mean of the CMIP6 models in which the NADW extends to a depth of about 3.1 km (Weijer et al. 2020; Roberts et al. 2020). The shallow NADW may result from the relatively poor vertical resolution of our models as suggested by Hirschi et al. (2020). The northward branch of the AMOC lower cell, which encompasses the Antarctic Bottom Water, is found at a shallower depth in all models than in observations, perhaps because our model doesn't extend as deep as the RAPID array. Still, the circulation at the bottom improves with increased horizontal resolution (Fig. 2) as found in Talandier et al. (2014).

### 3) Preindustrial control state of the AMOC

The pattern, intensity, and variability of the total AMOC in the preindustrial control run vary across the CM2-O suite, discussed here in both depth and density coordinates. As noted above, the upper cell ranges from 12 to 18 Sv across the CM2-O suite and has a depth (measured where the streamfunction is zero) of about 3 km (Fig. 3a-c). Below, the much weaker lower cell has a maximum of about -2 Sv in the MR and HR configurations and even less in the LR. The discrepancy in the maximum of the upper cell between the AMOC computed in depth and density coordinate is greatest in the subpolar gyre (Fig. 3g-i). Between 40°N and 50°N, the AMOC strength in depth




Accepted for publication in *Journal of Climate*. DOI 10.1175/JCLI-D-22-0561.1.

coordinates decreases significantly in our HR and MR configurations while the decrease occurs north of 50°N in the LR. This suggests that significant water mass transformation and sinking are taking place at lower latitudes in the MR and HR compared to the LR.

The AMOC in density coordinates is presented in Figure 3d-f to account for the transformation of buoyant water to dense water in the subpolar gyre that causes the sloping of isopycnals and leads to misinterpretation of the measured streamfunction in depth coordinates (Lozier et al. 2019). The upper cell of total AMOC in density coordinates is mainly found between isopycnal 35 to 37 kg/m$^3$. Below that density range, the lower cell does not appear. Above that density range, a counter-clockwise cell and a clockwise cell are found separated by the equator. These cells result from the Ekman transport driven by the Trade winds. In MR and HR, a stronger AMOC is found in density coordinates than in depth coordinates north of 40°N (Fig. 3g-i). This difference results from the projection in density space of a more vigorous and realistic subpolar gyre with water masses going north and south at the same depth, but with contrasting densities (Hirschi et al. 2020, see their Fig. 6).

There are large differences in the preindustrial AMOC variability across the CM2-O suite (Fig. 4). When computed at each grid point (in latitude, depth space), the variability from yearly-averaged time-series in the LR is twice as strong as in the MR and HR and it reaches a maximum of about 2.75 Sv around 40°N (Fig. 5). In comparison, Hirschi et al. (2020) found a maximum of about 1 to 2 Sv in their ocean models between 20-50°N with no clear conclusion on the effect of resolution at that scale (see their figure 7), while Delworth and Zeng (2012) found a more pronounced variability in CM2.1, the GFDL model that was used to develop the CM2-O suite (Delworth et al. 2012), compared to CM2.5 (see their figure 25).

Next, we isolate the inter-annual and decadal variability from the time-series. To isolate the inter-annual time-series, we have removed the 5-year moving average from the un-detrended time-series. We do not need to remove the model drift as it is included in the moving average. We found a standard deviation of about 62 to 72 meters for the upper cell depth metric and about 0.5 to 0.6 Sv for the AMOC strength. Thus, the inter-annual variability is similar across the CM2-O suite. In contrast, the decadal variability, which is given by the standard deviation of the 5-year moving average, is very different across model configurations. While the decadal variability is, for the MR and HR, 85 and 50 meters and 0.4 and 0.5 Sv, it is much larger in the LR configuration with a





Accepted for publication in *Journal of Climate*. DOI 10.1175/JCLI-D-22-0561.1.

standard deviation of about 152 meters and 2.0 Sv. This large decadal variability in the LR has a cycle of about 20 years and is also identified at 20°N in CM2.1 (Delworth et al. 2012; Delworth and Zeng 2012). Possible mechanisms for this variability include a westward propagation of subsurface temperature anomalies (Frankcombe et al. 2010) and the North Atlantic Oscillation (Delworth and Zeng 2016). This multi-decadal variability would deserve further investigation but the length of our simulations is too short to determine the significance and causes of it (only 4 cycles over the simulation). We now turn to the investigation of the AMOC response to climate change in our model suite.

## 3. AMOC response to Increased Carbon Dioxide Concentration

### *a. Response of the AMOC across the CM2-O suite*

In response to $CO_2$ forcing, our LR and HR configurations show an important shoaling of the AMOC upper cell of about 73 and 76 meters per decade, respectively, while the MR shows a modest reduction of 16 meters per decade (Fig. 4). Similarly, the AMOC weakening is substantial in our LR and HR configurations with a rate of -0.7 and -0.5 Sv per decade, respectively, which corresponds to a decline of about 37 and 27% in 80 years. This rate of decline is consistent with the estimated decline of 24-39% for the average of the years 2081–2100 relative to the historical period (1850–2014) from all forcing scenarios of the CMIP6 models (Weijer et al. 2020). In the MR, the AMOC strength does not show any sensitivity to the $CO_2$ forcing with the time-series of the two runs being statistically indistinguishable. This result is at odds with that of Jackson et al. (2020) who found a stronger response of the AMOC in their MR than in their LR model. However, it is consistent with Delworth et al. (2012) and Winton et al. (2014), two studies using the same model and configuration as our MR configuration (slightly different scenario runs) and other GFDL models. In Winton et al. (2014), the response of the AMOC to a doubling in atmospheric $CO_2$ concentration in the MR model is the weakest of all the models analyzed with a weakening of less than 2 Sv at 41°N. As most models analyzed by Winton et al. (2014) show a weakening of at least 3 Sv at this latitude, it suggests an unusual response in the CM2-O suite MR configuration.

The weakening of the AMOC is accompanied by a reduction in the inter-annual variability in all CM2-O suite model configurations (Fig. 5d-f) as well as in the multi-decadal variability for the





Accepted for publication in *Journal of Climate*. DOI 10.1175/JCLI-D-22-0561.1.

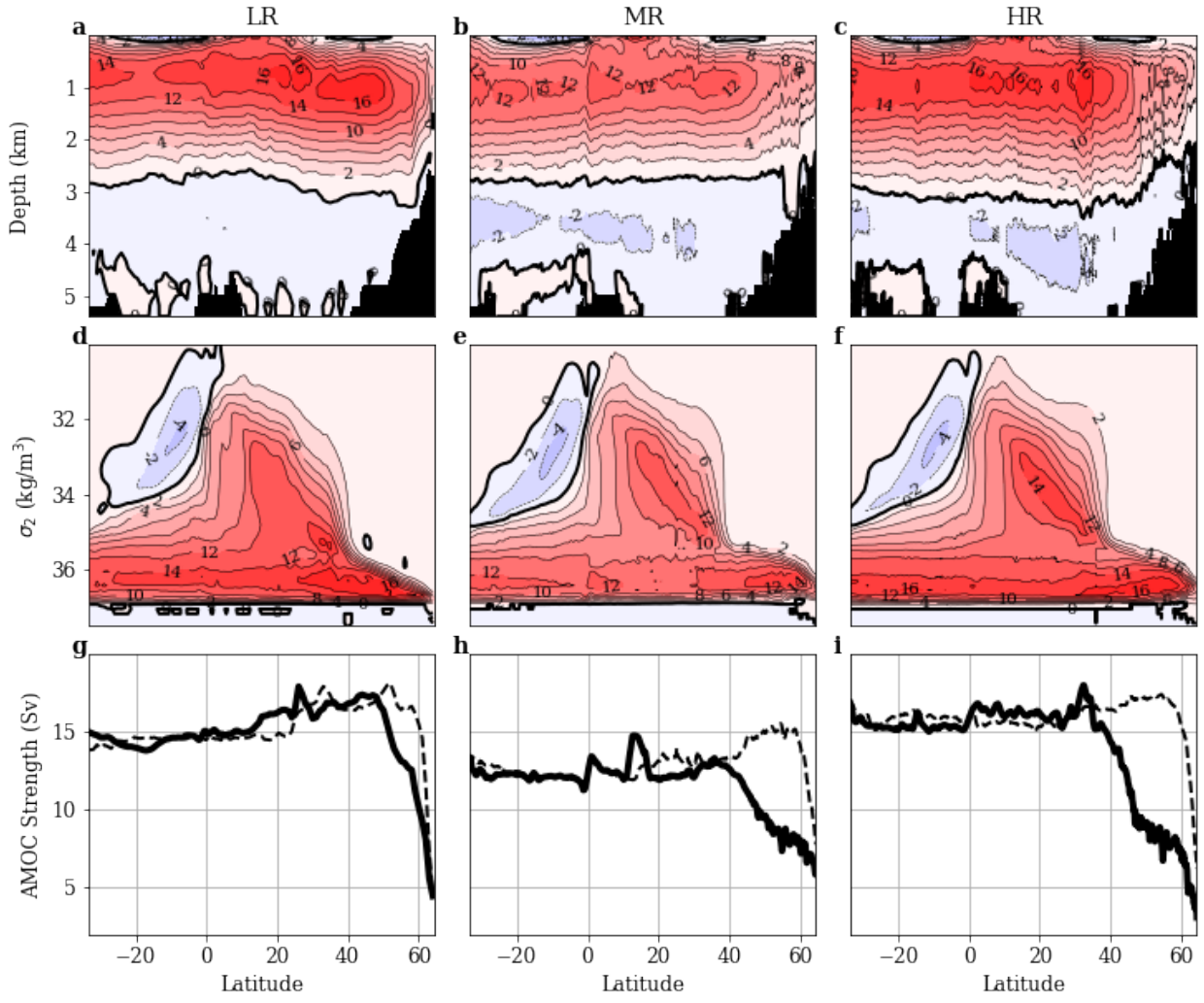


FIG. 3. Total AMOC averaged over the last 20 years of the CM2-O preindustrial control runs in depth coordinates (top panels) and in potential density referenced to 2 km ($\sigma_2$) coordinates (middle panels). Positive (red) contours indicate a clockwise circulation and negative (blue) contours indicate a counter-clockwise circulation. Contour intervals are 2 Sv and the bold line is the zero contour. The black area is topography. The bottom panels show the maximum AMOC strength (i.e., the maximum overturning over the water column) at each latitude for the AMOC in depth coordinates (thick solid lines) and in $\sigma_2$ coordinates (thin dashed lines).

LR (Fig. 4d). This strong reduction in the AMOC multi-decadal variability under global warming was also noted by Cheng et al. (2016) in an analysis of a subset of CMIP5 models.





Accepted for publication in *Journal of Climate*. DOI 10.1175/JCLI-D-22-0561.1.

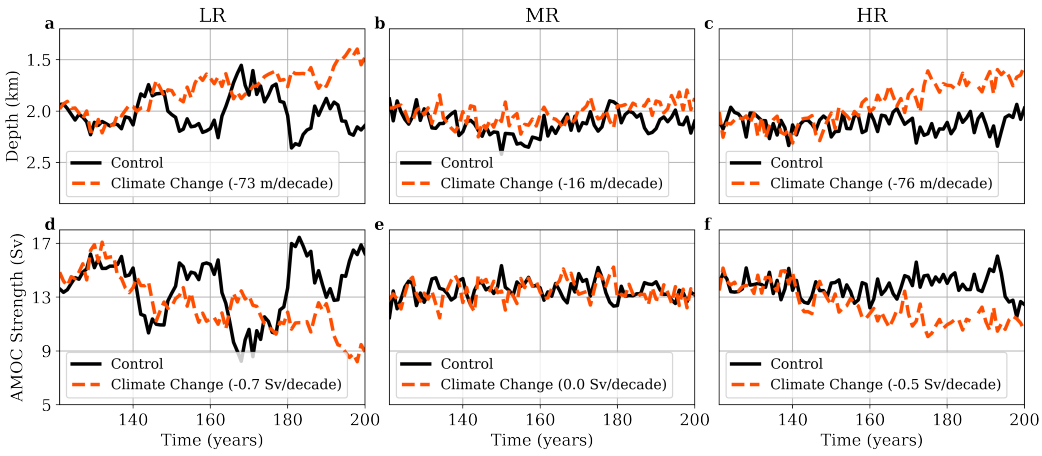


FIG. 4. Time-series of the total AMOC characteristics averaged between 30 and 50°N. The model drift has been removed and the climate change trends indicated in the legends are statistically significant only for the LR and HR. (a-c) Upper cell vertical extent proxy. To follow the depth of the AMOC upper cell in time, we use the depth below 1 km at which the AMOC strength is half of the AMOC strength at year 121, which is the year when the climate change runs branches off from the control runs. We use this metric because it allows us to see changes in the AMOC vertical structure, while there is little change in the depth at which the streamfunction is maximum even if the vertical extent of the cell reduces. We also do not use the depth at which the streamfunction is zero because the lower cell is not well-defined in the LR configuration. The AMOC is interpolated from the coarse model vertical grid to a vertical resolution of 1 meter to determine the depth with accuracy. (d-f) AMOC strength (maximum over the water column in depth coordinates).

### *b. Contribution from the mesoscale eddy component*

We first present an overview of the spatial pattern of the mesoscale eddy component before investigating its contribution to the AMOC response to climate change at 40°N. We focus our investigation on 40°N because it is representative of the total AMOC over most of the basin (Fig. 3) and because the mean state and response of the eddy streamfunction are stronger and better defined between 35 to 65°N. Our choice of latitude is also motivated by the fact that mesoscale eddies are not well-resolved poleward of 50° in the HR configuration. An analysis of the latitude dependence and the choice of 40°N is presented in the supplementary material.In addition, a density coordinate framework is used to investigate the contribution of mesoscale eddies to the





Accepted for publication in *Journal of Climate*. DOI 10.1175/JCLI-D-22-0561.1.

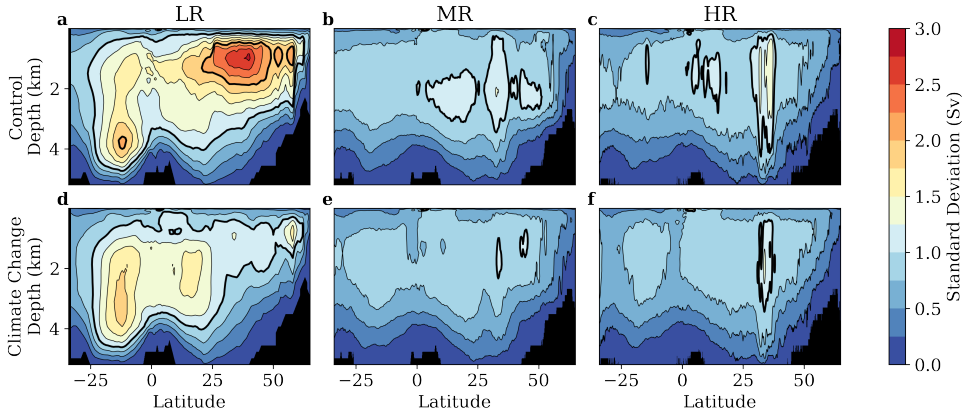


FIG. 5. Standard deviation of the AMOC strength (Sv) across the CM2-O suite. The standard deviation is computed from yearly averages over the last 80-years of the runs. The top row shows the control runs and the bottom row shows the climate change runs. For all runs, the local linear trend was removed at each grid cell before the computation of the standard deviation. The contour interval is 0.25 Sv. The thick black lines indicate the 1 Sv and 2 Sv contours. The black area is the topography.

AMOC as mesoscale eddies tend to stir and transport tracers along isopycnal surfaces (e.g., Gent et al. 1995).

In the control runs, the spatial pattern of the mesoscale eddy component is different than that of the total AMOC. Recall that the total AMOC in density coordinates has a clockwise circulation for most of the basin and a counterclockwise circulation in the surface tropical South Atlantic Ocean (Fig. 3d-f). Mesoscale eddy circulation enhances the clockwise circulation in the subpolar gyre between latitudes 40 and 65°N within a density ranging from 35 to 37 kg/m$^3$ (Fig. 6a-c). Conversely, mesoscale eddy streamfunction opposes the clockwise circulation in the tropical North Atlantic (not shown).

The response of the mesoscale eddy component to the $CO_2$ increase is mostly localized in the subpolar gyre. Between 40 and 65°N, both the LR and HR exhibit a decrease in mesoscale eddy streamfunction within a density ranging from 35 to 37 kg/m$^3$ (Fig. 6d-f). Also, there is an increase in mesoscale eddy streamfunction slightly above that density range due to the decrease in density of the upper North Atlantic waters in the climate change scenario, which is most pronounced in the HR. In the MR, mesoscale eddy streamfunction response is of small amplitude and does not show a well-defined spatial pattern.





Accepted for publication in *Journal of Climate*. DOI 10.1175/JCLI-D-22-0561.1.

At 40°N in the control run, the maximum mesoscale eddy contribution to the upper cell is found to be about 2 Sv in the LR and MR and peaks at 5 Sv at 35.4 kg/m$^3$ in the HR (Fig. 7 a-c). To quantify the mesoscale eddy contribution to the total AMOC at 40°N, we compute the weighted integral of both mesoscale and total streamfunctions over the upper cell, defined here to be between 35 kg/m$^3$ and the isopycnal where the total AMOC is zero. The results are not sensitive to the upper limit here as densities lighter than 35 kg/m$^3$ do not occupy a lot of space vertically (Fig.7e,j).

As expected, we found that the mesoscale eddy contributes more to the total AMOC in the HR configuration than in its lower-resolution counterparts. More specifically, the mesoscale eddy contribution accounts for about 6-7% of the total AMOC in the LR and MR and about 9% in the HR (Table 1). The mesoscale eddy contribution to the total AMOC is reduced in the climate change scenario (Fig. 7 f-h) and accounts for about 5% of the total AMOC in the LR and MR, and 7% in the HR (Table 1). This means that the mesoscale eddy streamfunction decreases proportionally more than the total streamfunction, which indicates its important role in the AMOC decline. Indeed, mesoscale eddy accounts for about 13% and 17% of the total AMOC response in the LR and HR. In the MR, the response of the mesoscale eddy is 65%, but we shall recall the lack of sensitivity of MR in its total AMOC response, i.e. the total AMOC response is small.

We note that the parameterization of mesoscale eddy ($\Psi^*_{GM}$; eq. 3) accounts for most of the total mesoscale eddy streamfunction in both control and climate change runs. Thus, the parameterization of mesoscale eddy transport enables the LR configuration to produce a mesoscale eddy streamfunction of similar magnitude as that resolved by our higher-resolution model configurations.





Accepted for publication in *Journal of Climate*. DOI 10.1175/JCLI-D-22-0561.1.

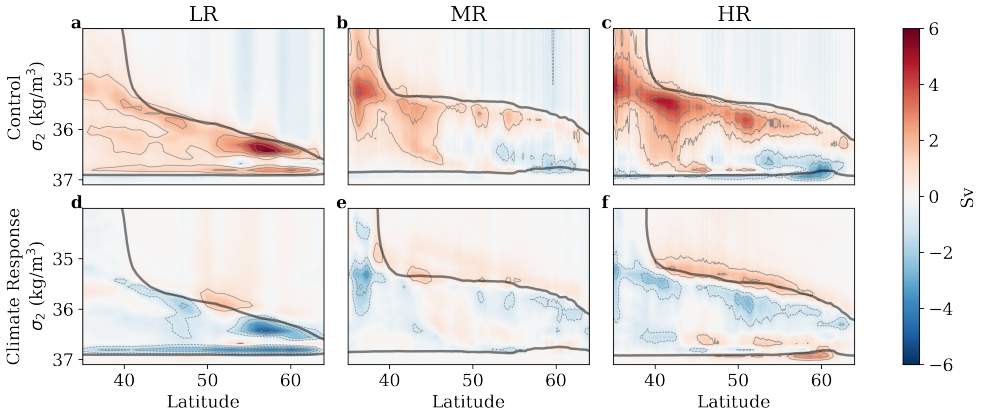


FIG. 6. Total mesoscale eddy streamfunction ($\Psi^*$, Eq. 3) for the control run (a-c) and the climate change response (d-f) in potential density coordinates referenced to 2 km ($\sigma_2$) for the CM2-O suite. Thin grey contours indicate $\Psi^*$ with an interval of 1 Sv except it does not show the zero contour. The bold black contour outlines the 2 Sv control total AMOC ($\Psi$) as in Fig. 3d-f.

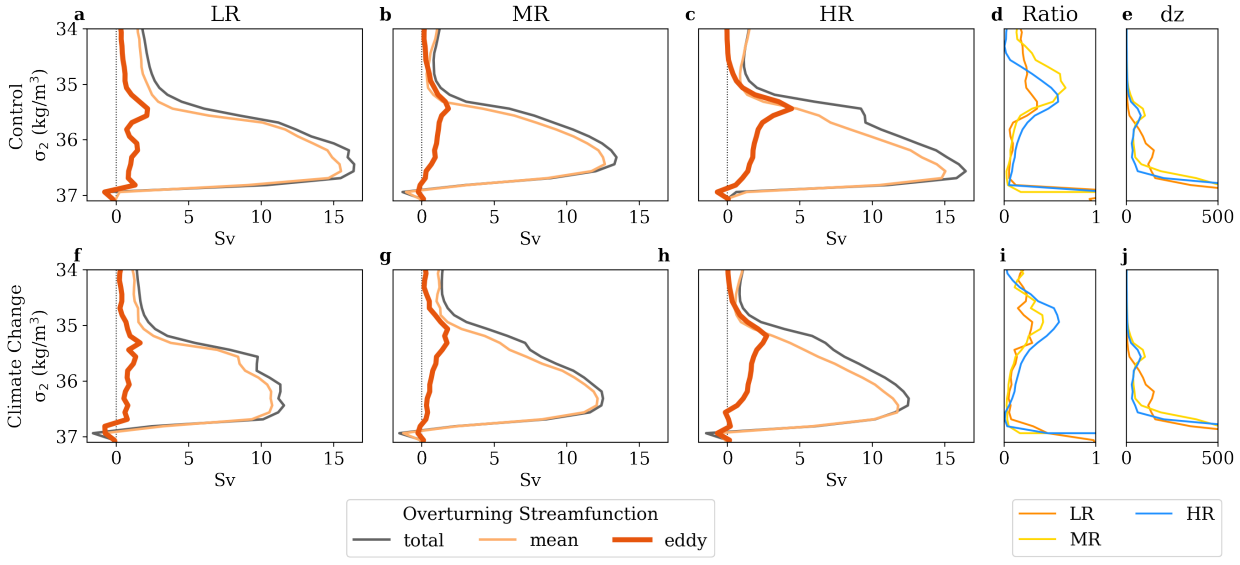


FIG. 7. (a-c, f-h) Total (thin dark grey), Eulerian-mean (thin light orange), and total eddy (bold dark orange) streamfunctions in potential density coordinates referenced to 2 km ($\sigma_2$) at 40°N, along with their mesoscale eddy ratio (d,i) and the vertical extent of each density bin (e,j), for the control (top) and change due to the climate change (bottom) in the CM2-O suite.





Accepted for publication in *Journal of Climate*. DOI 10.1175/JCLI-D-22-0561.1.

TABLE 1. Weighted integrated sum ratio (%) over the density range going from 35 kg/m$^3$ to where AMOC total is zero in the CM2-O suite. We computed the integrated sum ratio for the control, climate change, and response streamfunctions. The difference is the difference between climate change and control ratios. LR (Total) includes the resolved and the parameterized eddy, while LR (GM) is only for the parametrized eddy.

| | LR (Total) | LR (GM) | MR | HR |
|---|---|---|---|---|
| Control | 7.2 | 5.3 | 6.4 | 9.1 |
| Climate Change | 5.2 | 5.2 | 5.5 | 7.3 |
| Difference | -2.0 | -0.1 | -0.9 | -1.8 |
| Response | 13.3 | 5.9 | 65.3 | 16.8 |

### *c. Contribution from the geostrophic component*

#### 1) RESPONSE OF THE GEOSTROPHIC COMPONENT TO CLIMATE CHANGE

Here, we examine the geostrophic AMOC which is a good approximation of the Eulerian-mean component in the upper cell (see Section 2.b.2). Indeed, in the CM2-O suite, the Eulerian-mean streamfunction accounts for the majority of the total AMOC and its decline (Fig. 7). We focus our investigation on 40°N to allow a comparison to the previous section on mesoscale eddy and also because we compute the geostrophic streamfunction in depth coordinates. As a reminder, the control AMOC in depth coordinates decreases strongly north of 40°N in the MR and HR models but not in density coordinates (3).





Accepted for publication in *Journal of Climate*. DOI 10.1175/JCLI-D-22-0561.1.

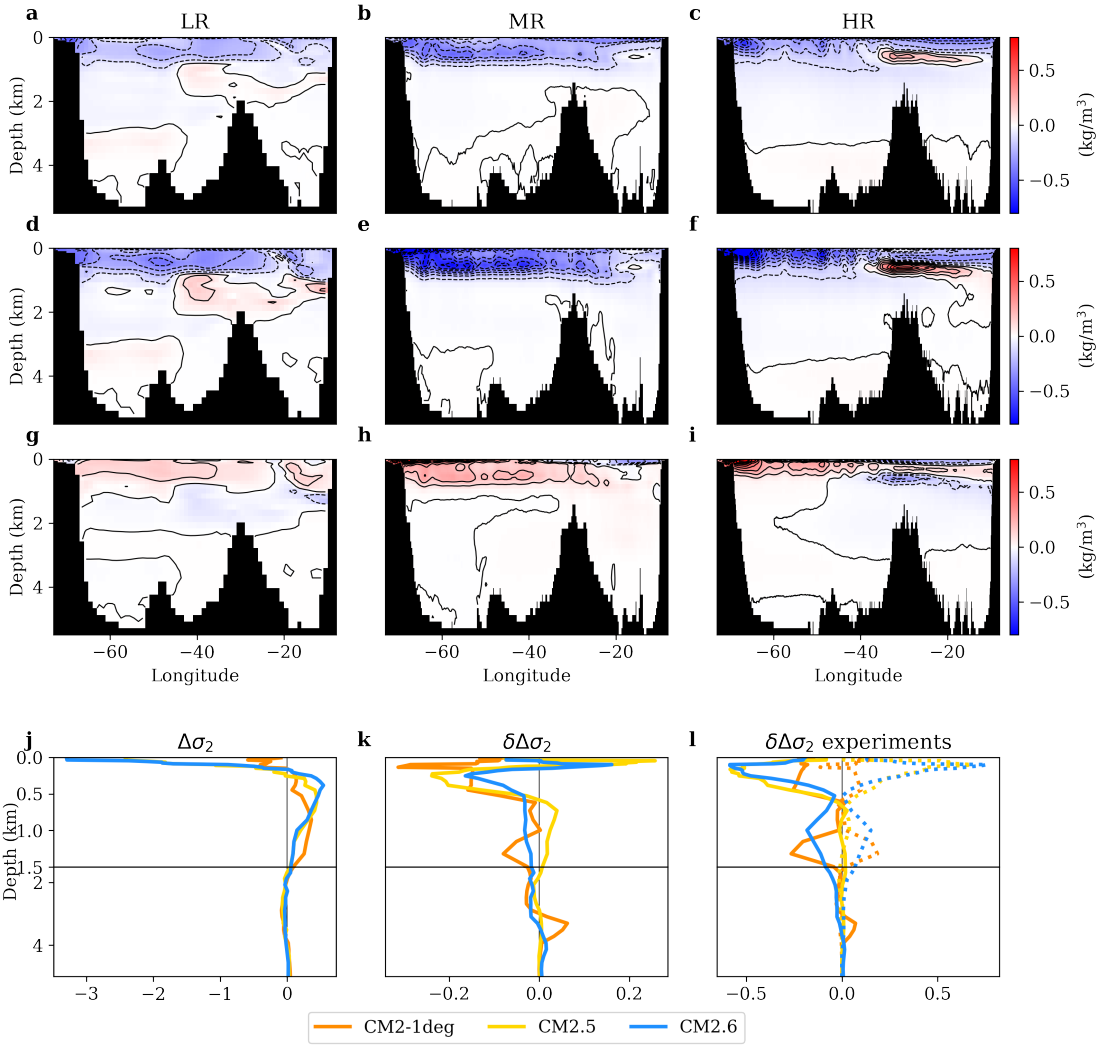


FIG. 8. The change in potential density referenced to 2 km ($\sigma_2$; a-c) averaged over the last 20 years of the runs at 40°N in the CM2-O suite and the contributions of temperature (d-f) and salinity (g-i) to the change in density. The black area is topography. (j) The control density gradient between the west and the east ($\rho_w - \rho_e$; eq. 5). Positive (negative) values correspond to a southward (northward) geostrophic transport. (k) The climate response of the density gradient. Negative values between ≈ 0.3 to 1.5 km indicate a reduction of the southward transport. (l) Change in the density gradient from the temperature-only (solid) and the salinity-only (dotted) response to climate change. Note the two minimums in the LR and HR (around 0.3 and 1 km) of the density gradient change for the temperature-only response.





Accepted for publication in *Journal of Climate*. DOI 10.1175/JCLI-D-22-0561.1.

As the geostrophic component of the AMOC is derived from the thermal wind relation, its climate response is tied to density anomalies. As a reminder, our geostrophic component is computed from the density gradient at the eastern and western basin margins. For the control runs, the density gradient ($\Delta\sigma_2 = \rho_w - \rho_e$; eq. 5) is negative for the top hundred of meters, positive below, and goes toward zero at about 1.5 km (Fig. 8j). This indicates a geostrophic northward flow in the upper branch of the upper cell and a southward flow in the lower branch of the upper cell.

The density anomalies caused by the $CO_2$ increase show some similarity across the CM2-O suite, such as a zonal asymmetry with greater and deeper loss in buoyancy in the west than in the east (Fig. 8 a-c). The zonal asymmetry leads to changes in the density gradient, which is most pronounced in the top 1 km but is present down to 3 km in particular in the LR and HR (Fig. 8 k). According to the thermal wind theory, the negative anomaly in the zonal density gradient causes an anomalous northward transport for the whole depth of the AMOC upper cell. As a result, the northward transport in the upper branch of the upper cell (top 1 km) increases while the southward transport of the lower branch of the upper cell (1-3 km) decreases. Because the lower branch of the upper cell is associated with a greater volume than the upper cell, overall, the upper cell strength of the AMOC decreases. In the MR, the decrease in density at the western margin is interspersed with a small increase in density at around 1 km. This positive anomaly opposes the decline in AMOC and leads to little change in the geostrophic AMOC component in that model configuration.

### 2) Role of temperature versus salinity in the response of the geostrophic AMOC

To refine our understanding of the response of the geostrophic AMOC to climate change, we separate the effect of temperature and salinity on the density anomalies. To do so, we compute the geostrophic AMOC using the salinity of the climate change run and the averaged temperature of the control run, and vice versa, for every year of the 80 years of the climate change run (Fig. 9).

The temporal variability of the salinity and temperature contributions to the geostrophic AMOC oppose each other with the magnitude of the contributions largely fluctuating, especially in the LR configuration. These fluctuations from temperature-only and salinity-only changes mostly cancel each other as the variability observed in the climate change run is much smaller. Additionally, there is no significant change in the sign of the salinity and temperature contributions in the MR and HR configurations.





Accepted for publication in *Journal of Climate*. DOI 10.1175/JCLI-D-22-0561.1.

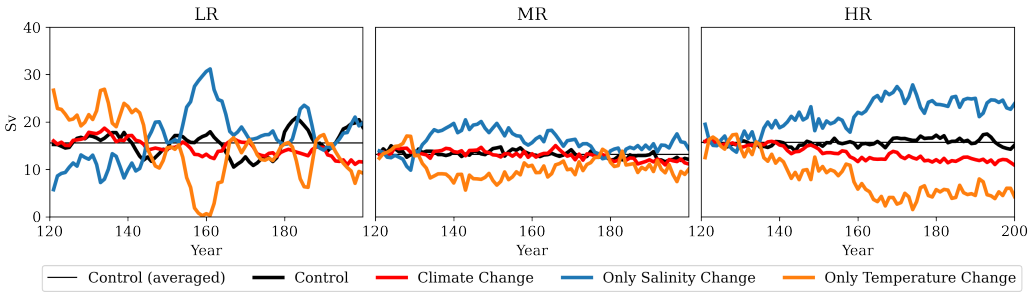


FIG. 9. Geostrophic AMOC strength calculated as the maximum in $\Psi_{geo}$ (eq. 6) at 40°N for different combinations of salinity- and temperature-driven density anomalies over years 121-200. Geostrophic AMOC computed with both salinity and temperature from (black line) the control run or (red line) the climate change scenario. Geostrophic AMOC from salinity changes only and averaged temperature from the control (blue line). Geostrophic AMOC from temperature changes only and averaged salinity from the control (orange line).

A common feature among all our model configurations is that the temperature change drives the decline of the geostrophic AMOC, while the salinity change acts to strengthen the geostrophic AMOC. Such compensating changes are to be expected as the temperature and salinity contribution to the density change are similar in spatial pattern but opposite in sign as it mostly consists of a warming and a salinification in the upper 1.5 km (Fig. 8 d-i). This compensation is also reflected in the density gradient change from temperature-only or salinity-only changes (Fig. 8 l).

In all model configurations, the waters over the top 1 km become warmer and saltier under climate change on the western side, with an overall decrease in density as the impact of temperature anomalies is stronger (Fig. 8a-c, k). The models also exhibit a surface warming on the eastern side, although more modest and extending only down to 0.5 km in the HR, with cooling between 0.5 to 1 km depth (Fig. 8d-f). The salinity changes also show some spatial heterogeneity on the eastern side with a freshening near the surface and an increase in salinity below (Fig. 8g-i). In the LR and HR configurations, a layer of freshening is found below a layer of salinity increase. An overall western intensified warming and increase in salinity over the top 1 km, accompanied by a surface freshening in the eastern side, were also described in the CMIP5 model mean following the radiative concentration pathway 8.5 (RCP8.5) scenario (Levang and Schmitt 2020).





Accepted for publication in *Journal of Climate*. DOI 10.1175/JCLI-D-22-0561.1.

## 4. Discussion

### *a. AMOC response*

In the CM2-O suite, a non-monotonic relation is found between horizontal resolution and the total AMOC response to $CO_2$ forcing. While the low-resolution (LR) and high-resolution (HR) configurations show similar AMOC weakening and shoaling rates, the medium-resolution (MR) stands out due to its lack of sensitivity to the $CO_2$ forcing (see Section 3a). Interestingly, a similar non-monotonic relation is found in another study of the CM2-O suite between horizontal resolution and the increase in ocean heat transport to the Arctic in response to $CO_2$ forcing (Decuypère et al. 2022). The authors showed that the MR receives more heat than its counterparts under climate change, resulting in a smaller Arctic sea ice extent. A comparison of the Arctic sea ice across the suite further revealed many similarities between the LR and HR, with the MR remaining the outlier.

The lack of sensitivity to the $CO_2$ forcing we found in the MR is particularly intriguing as the prescribed $CO_2$ increase (1% per year) is expected to lead to a decline in its AMOC. The forcing used in this study corresponds to an intermediate scenario between the radiative concentration pathways RCP6.0 and RCP8.5, which are scenarios of a world where no additional effort to constrain emissions is made (Pachauri et al. 2014). The AMOC weakening is a consistent feature in all future emissions scenarios across both CMIP5 and CMIP6 models, although its magnitude varies across models (Collins et al. 2013; Weijer et al. 2020). The decline of about 37% in the LR and of 27% in the HR is comparable to the decline of 36% for the RCP8.5 scenario in CMIP5 models and of 39% for the Shared Socioeconomic Pathways 5-8.5 (comparable to RCP8.5) in CMIP6 models.

The MR also stands out by having a weaker AMOC in the control run than the LR and HR, which have comparable AMOC strengths as the CMIP5 model-mean (Fig. 3; Hirschi et al. 2020). At 40°N, the AMOC strength in the MR is 80% of that in LR and HR in both depth and density coordinates. The weak control AMOC and associated weak response in the MR is in good agreement with several papers which found such a relationship across a variety of climate models (Winton et al. 2014; Jackson et al. 2020; Weijer et al. 2020) although Weijer et al. (2020) cautioned that the relationship was not reproduced by all CMIP6 models. Winton et al. (2014) describes





Accepted for publication in *Journal of Climate*. DOI 10.1175/JCLI-D-22-0561.1.

a strong relationship between the strength of the preindustrial control AMOC (at 41°N) and its decline under a doubling of $CO_2$ in ten GFDL models. That is, GFDL models with a stronger control AMOC show a stronger decline under $CO_2$ forcing. Interestingly, the AMOC strength in the preindustrial run of the HR model used in Winton et al. (2014), which is the same HR model configuration as we use, is about 12 Sv, similar to our MR. These differences in AMOC strength may arise from the comparison of single realizations of these climate models, that is, there may be significant variability between realizations. Indeed, a study on the sensitivity of the AMOC to the ocean resolution shows a large spread within subgroups of different ocean resolutions (Roberts et al. 2020, see their figure 9). Additionally, the authors conclude that the AMOC response tends to be stronger as ocean model resolution is enhanced, a conclusion that we can not contradict as our study comprises only 3 different ocean model resolutions. Although computationally expensive, a model ensemble of the CM2-O suite would provide a better estimate of the difference in AMOC strength and variability across the suite.

*b. Mesoscale eddy representation and its contribution to the total AMOC response*

The decomposition of the total AMOC in its eddy and Eulerian-mean components allowed us to quantify the exact contribution of the mesoscale eddy streamfunction to the total AMOC and its response (Table. 1). At 40°N, the mesoscale eddy streamfunction accounts for 6 to 9% of the total AMOC in the control run and is reduced to 5 to 7% in the climate change run. We note that the eddy contribution is of similar magnitude in the LR and MR configurations, meaning that the eddy parameterization compensates for the lack of representation of mesoscale eddies in the coarsest configuration of the suite. Also, as expected, the HR has the largest contribution of the mesoscale eddy in both runs. The mesoscale eddy component contributes significantly to the total AMOC response to $CO_2$ increase in the CM2-O suite by about 13% in the LR and 17% in the HR. Note that we disregarded the MR due to the lack of sensitivity of its total AMOC to the $CO_2$ forcing. The HR thus presents the strongest mesoscale eddy contribution of the CM2-O suite both in the runs and in the response to the $CO_2$ forcing. However, even our HR model is not eddy-resolving poleward of 50°N. Hence, there is a possibility that a larger fraction of the total AMOC and its response would be accounted for by mesoscale eddy in an even higher resolution model. Thus,




Accepted for publication in *Journal of Climate*. DOI 10.1175/JCLI-D-22-0561.1.

more investigation of the mesoscale eddy contribution is needed in high and very high-resolution models to assess their role in the AMOC response to climate change.

*c. How water properties anomalies propagation shape the AMOC response*

Despite the significant contribution of the mesoscale eddy component to the AMOC response, the contribution of the Eulerian-mean component is largely dominant. This component is mostly geostrophic and its response to the $CO_2$ forcing is driven by temperature changes rather than salinity changes (Section 3c2), in agreement with Levang and Schmitt (2020). As noted in Section 3c, the density decrease at 40°N in response to a $CO_2$ increase is greater in the west. Comparing the western and eastern contributions indicates that geostrophic AMOC decline is mainly driven by changes at the western boundary with an opposite effect of the eastern boundary (not shown). Thus, we next discuss the processes that may cause the density anomalies along the western boundary at 40°N.

As the concentration of $CO_2$ increases in the CM2-O suite, the surface air temperature warms and the freshwater fluxes (evaporation minus precipitation) pattern is enhanced over the North Atlantic Ocean (Fig. S1). The density of the surface ocean is directly impacted through exchanges with the atmosphere and indirectly through the melting of ice sheets and reduced sea-ice formation. These anomalies can easily reach great depths in the North Atlantic deep water formation regions and then can be advected at depth. To pinpoint where the density anomalies originate, we can associate the temperature and salinity anomalies found at depth along the western boundary at 40°N with the surface temperature and salinity response. As the atmosphere is warmer over the whole Atlantic Ocean, salinity is a better indicator of the anomalies' origin.

In the subtropics, enhanced evaporation under $CO_2$ forcing causes a positive salinity anomaly at the sea surface. Levang and Schmitt (2020) suggest that the salty surface waters from the subtropics, that are advected northward along the western boundary, subduct and mix with the NADW where the streamlines of the AMOC outcrop between 15 and 30°N (Fig. 8 of Levang and Schmitt 2020, and our Fig. 3). The density anomalies could also originate from the deep-water formation regions in the North Atlantic where enhanced precipitation causes a negative salinity anomaly at the sea surface, then subducts in the deep mixed layer and propagates southward along the DWBC. Waldman et al. (2020) demonstrate how the Labrador Sea waters and Arctic waters





Accepted for publication in *Journal of Climate*. DOI 10.1175/JCLI-D-22-0561.1.

that are exported through the Davis Strait can propagate anomalies southward along the western boundary within the NADW in the CNRM-CM6.

The configurations of the CM2-O suite have different salinity responses along the western boundary at 40°N, but they all show an increase in salinity over the upper 1.5 km (Fig. 8g-i). This suggests that the upper 1.5 km is strongly impacted by atmospheric changes over the subtropical region. Below 1.5 km the salinity changes are of smaller magnitude, which suggests that these waters are mixed with older water or that salinity anomalies from the subtropical and subpolar regions oppose each other. Note that in MR the salinity anomalies below 1.5 km are negative, in HR they are positive, and in LR they oscillate between the two. In addition to the anomalies, the density response in the western boundary at 40°N could be due to circulation changes (Holliday et al. 2020). Indeed the Labrador Sea Water advected southward is very cold and fresh compared to the subtropical waters. Next, we discuss the connectivity between the northern deep-water formation regions and the western boundary through the DWBC.

In the North Atlantic, the NADW is characterized by a maximum in dissolved oxygen and a minimum in normalized age tracer, meaning that these waters have been in recent contact with the surface. These characteristics, which can be found throughout the whole water column in the Labrador Sea where the water is ventilated (Fig. 10, sections between 55°N and 60°N), are found far from the subpolar convection sites at about 2 km depth mostly on the western side of the Atlantic basin (Fig. 10, sections between 35°N and 45°N). Thus, Labrador Sea characteristics can be found at mid-latitudes as it advected southward as the NADW. In LR, the NADW is mainly found to the west of the Mid-Atlantic Ridge south of 50°N in good agreement with observations (Schlitzer 2000), while in MR and HR, the NADW is found on both sides of the Mid-Atlantic Ridge. The presence of NADW away from the DWBC is linked to two major interior pathways: a southward interior pathway towards the subtropics and a northeastward interior pathway at the boundary between the subpolar and subtropical gyres within the North Atlantic Current. Both pathways have been observed (Bower et al. 2009) and documented in models (Zhang 2010; Zhang et al. 2011). At 35°N, however, the dissolved oxygen maximum does not appear anymore in MR and the minimum age tracer is centred above the Mid-Atlantic Ridge (Fig. 10, section 35°N), indicating that all of the NADW have followed a northeastern route. This major rerouting of the NADW suggests a strong recirculation branch in MR. Both MR and HR show a stronger subpolar and subtropical gyre





Accepted for publication in *Journal of Climate*. DOI 10.1175/JCLI-D-22-0561.1.

circulation than LR with a boundary between the two gyres reaching 45°N, extending further south than in their coarser-resolution counterpart (Fig. 11). Though the recirculation is strongest in HR, the southward circulation around the tip of Grand Banks associated with the DWBC is vigorous enough to bring the NADW to lower latitudes (Figs. 10 and 11). However, in the MR, the water does not seem to leak southward and is essentially trapped in the subpolar gyre. This is a possible explanation for the lack of connection between the subpolar and subtropical gyres in MR.

The weaker AMOC in MR control simulation may result from the stronger recirculation of the NADW which may reduce the southward volume export. The recirculation of the NADW in MR also prevents the spreading of the density anomalies from the convection sites to lower latitudes of the North Atlantic basin. Hence, despite a reduction of deep convection under climate change of similar magnitude across the CM2-O suite (not shown), the density change along the western side of the basin remains close to zero at 40°N in the MR, leaving the geostrophic component at that latitude unchanged too. Given the predominance of the geostrophic component in the response of the AMOC to climate change, we thus postulate that the lack of sensitivity of the AMOC to climate change in our MR is due to a weak connection between the subpolar and subtropical circulations. A weak connection between the Labrador Sea and the subtropical gyre through the export of deep waters within the DWBC is supported by some observational (e.g. Bower et al. 2009) and modelling studies (e.g. Zou and Lozier 2016; Zou et al. 2019), but uncertainties on its strength and variability remain. As our results suggest a key role for this connection in setting the intensity of the response of the AMOC to climate change, a closer examination of the representation of this connection in climate models appears desirable when investigating changes in the AMOC.





Accepted for publication in *Journal of Climate*. DOI 10.1175/JCLI-D-22-0561.1.

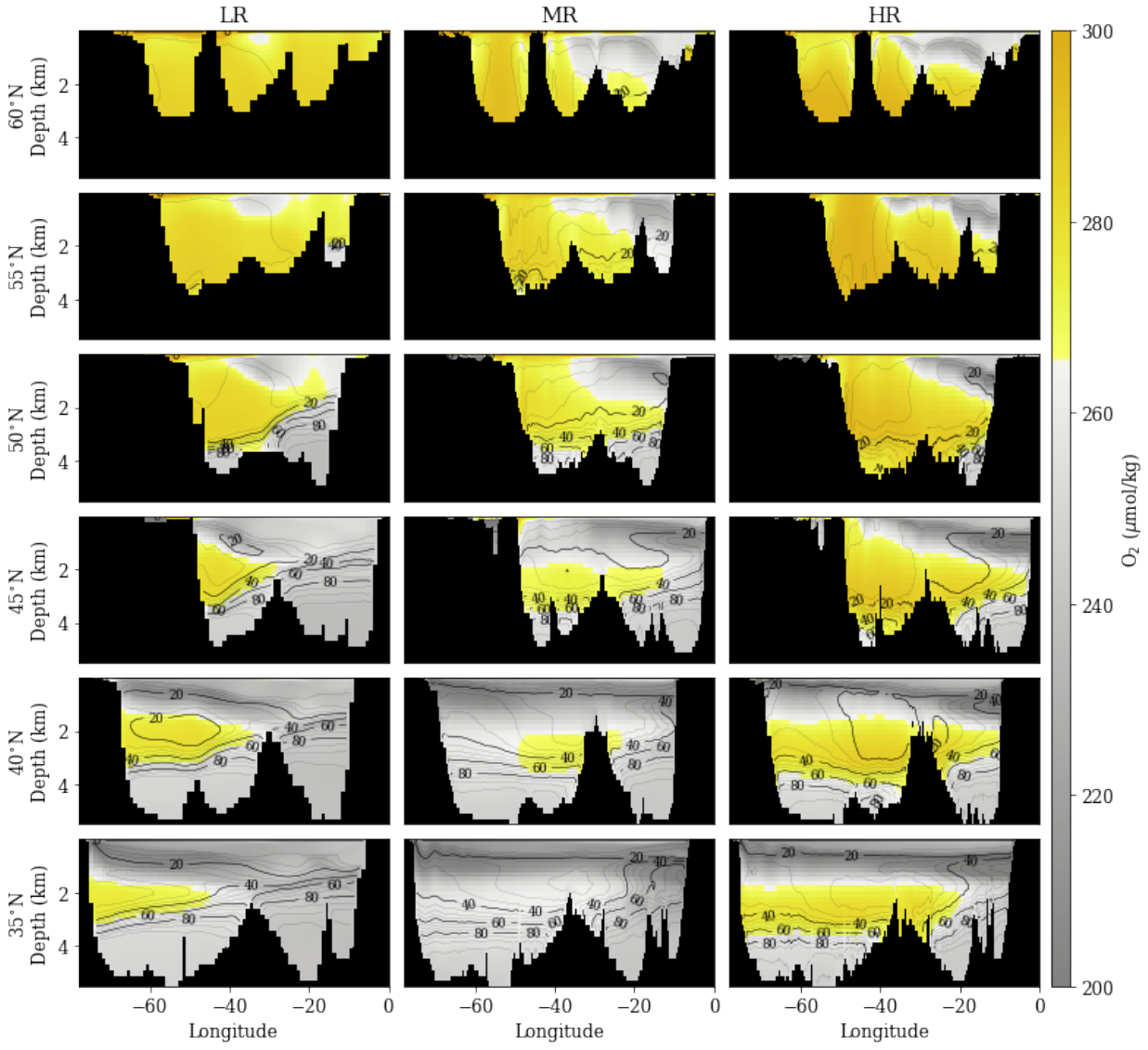


FIG. 10. Dissolved oxygen ($\mu$mol/kg) maximum (yellow colours) and minimum (grey colours), along with the normalized age tracer contours with intervals of 5 years (grey contours) and 20 years (black contours). The normalized age tracer indicates recently ventilated (young) waters and unventilated (old) waters. Outputs are averaged over the last 20 years of the control runs at various latitudes in the CM2-O suite. The black area is topography.





Accepted for publication in *Journal of Climate*. DOI 10.1175/JCLI-D-22-0561.1.

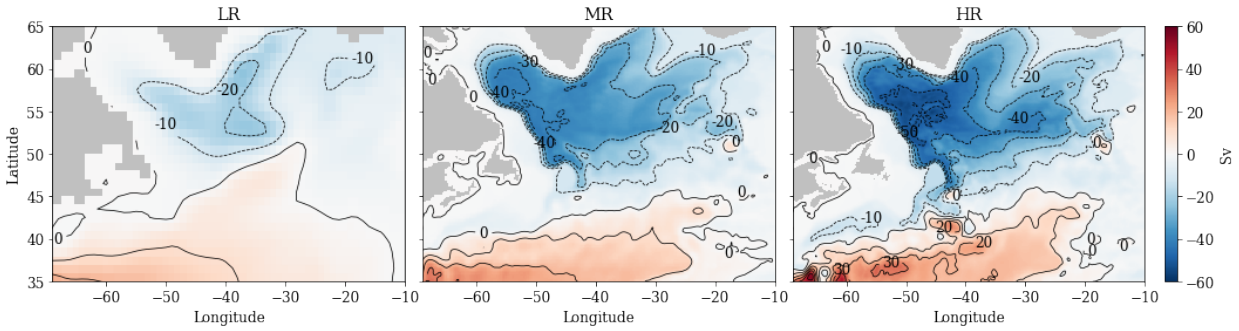


FIG. 11. Barotropic Quasi Streamfunction for the CM2-O model suite, averaged over the last 20 years of the control runs. The grey area is topography

## 5. Summary

In this study, we investigated the response of the AMOC to a doubling in the atmospheric $CO_2$ concentration in a hierarchy of three coupled climate model configurations. The decomposition of the AMOC into its drivers revealed that:

1. The magnitude of the AMOC weakening is related to its control strength as demonstrated by Winton et al. (2014), Jackson et al. (2020), and Weijer et al. (2020); the stronger the AMOC in the control run, the stronger its response to $CO_2$ forcing.

2. The response of the AMOC to increasing $CO_2$ forcing has a non-monotonic behavior along the horizontal resolution axis of our model suite. While the LR and HR show similar responses, the MR shows a lack of sensitivity to the forcing.

3. Changes in the mesoscale eddy streamfunction contribute to approximately 13 to 17% of the AMOC decline in the LR and HR.

4. The upper cell of the control AMOC and its response can be approximated by the geostrophic component. Thus, the density response governs the AMOC response.

5. The salinity-driven response of the geostrophic AMOC partially opposes that of the temperature-driven response, albeit with a smaller magnitude. At the decadal time scale considered in this study, it is the temperature anomalies at the basin margins that drive the geostrophic AMOC response, in a consistent way across the CM2-O suite.




Accepted for publication in *Journal of Climate*. DOI 10.1175/JCLI-D-22-0561.1.

6. In the MR, the strong recirculation of newly formed deep waters within the subpolar gyre indicates a weak connection between deep-water production sites and the subtropical gyre through the DWBC. This weak connection might lead to a weak AMOC control state and response to a strong $CO_2$ forcing.

## 6. Acknowledgements

A.-S.F. acknowledges the financial support from Hydro-Québec, the National Sciences and Engineering Research Council of Canada (NSERC) through the Discovery grant and Accelerator supplement [RGPIN-2018-04985], the Fonds de Recherche du Québec Nature et Technologie and McGill University, and the scientific support from the Québec Océan strategic cluster. RM acknowledges funding from the European Union as part of the EPOC project (Explaining and Predicting the Ocean Conveyor). Views and opinions expressed are however those of the author(s) only and do not necessarily reflect those of the European Union. Neither the European Union nor the granting authority can be held responsible for them. We thank the Geophysical Fluid Dynamics Laboratory for sharing the model output of the CM2-O suite, and Louis-Philippe Nadeau and Samuel Levang for helpful discussions.

## 7. Data availability

Data from the RAPID MOC monitoring project are funded by the Natural Environment Research Council and are freely available from www.rapid.ac.uk/rapidmoc. Data from the WOA are freely available from https://accession.nodc.noaa.gov/NCEI-WOA18. The numerical model simulations upon which this study is based are too large to archive or transfer. Some output can be made available upon request.

## References

Bailey, D. A., P. B. Rhines, and S. Häkkinen, 2005: Formation and pathways of North Atlantic Deep Water in a coupled ice–ocean model of the Arctic–North Atlantic Oceans. *Climate dynamics*, **25 (5)**, 497–516.

Bellomo, K., M. Angeloni, S. Corti, and J. von Hardenberg, 2021: Future climate change shaped by inter-model differences in Atlantic meridional overturning circulation response.





Accepted for publication in *Journal of Climate*. DOI 10.1175/JCLI-D-22-0561.1.

*Nature Communications*, **12**, 3659, https://doi.org/10.1038/s41467-021-24015-w, URL https://doi.org/10.1038/s41467-021-24015-w.

Boers, N., 2021: Observation-based early-warning signals for a collapse of the Atlantic Meridional Overturning Circulation. *Nature Climate Change*, **11**, 680–688, https://doi.org/10.1038/s41558-021-01097-4, URL https://doi.org/10.1038/s41558-021-01097-4.

Bower, A. S., M. S. Lozier, S. F. Gary, and C. W. Böning, 2009: Interior pathways of the North Atlantic meridional overturning circulation. *Nature*, **459 (7244)**, 243–247.

Buckley, M. W., and J. Marshall, 2016: Observations, inferences, and mechanisms of the Atlantic Meridional Overturning Circulation: A review. *Reviews of Geophysics*, **54 (1)**, 5–63.

Cheng, J., Z. Liu, S. Zhang, W. Liu, L. Dong, P. Liu, and H. Li, 2016: Reduced interdecadal variability of Atlantic Meridional Overturning Circulation under global warming. *Proceedings of the National Academy of Sciences*, **113 (12)**, 3175–3178.

Collins, M., and Coauthors, 2013: Long-term climate change: projections, commitments and irreversibility. *Climate Change 2013-The Physical Science Basis: Contribution of Working Group I to the Fifth Assessment Report of the Intergovernmental Panel on Climate Change*, Cambridge University Press, 1029–1136.

Danabasoglu, G., S. G. Yeager, Y.-O. Kwon, J. J. Tribbia, A. S. Phillips, and J. W. Hurrell, 2012: Variability of the Atlantic meridional overturning circulation in CCSM4. *Journal of climate*, **25 (15)**, 5153–5172.

Danabasoglu, G., and Coauthors, 2014: North Atlantic simulations in coordinated ocean-ice reference experiments phase II (CORE-II). Part I: mean states. *Ocean Modelling*, **73**, 76–107.

Decuypère, M., L. B. Tremblay, and C. O. Dufour, 2022: Impact of Ocean Heat Transport on Arctic Sea Ice Variability in the GFDL CM2-O Model Suite. *Journal of Geophysical Research: Oceans*, **127**, e2021JC017 762, https://doi.org/https://doi.org/10.1029/2021JC017762.

Delworth, T. L., and F. Zeng, 2012: Multicentennial variability of the Atlantic meridional overturning circulation and its climatic influence in a 4000 year simulation of the GFDL CM2.1 climate model. *Geophysical Research Letters*, **39 (13)**.





Accepted for publication in *Journal of Climate*. DOI 10.1175/JCLI-D-22-0561.1.

Delworth, T. L., and F. Zeng, 2016: The impact of the North Atlantic Oscillation on climate through its influence on the Atlantic meridional overturning circulation. *Journal of Climate*, **29 (3)**, 941–962.

Delworth, T. L., and Coauthors, 2012: Simulated Climate and Climate Change in the GFDL CM2.5 High-Resolution Coupled Climate Model. *Journal of Climate*, **25 (8)**, 2755–2781.

Dufour, C. O., and Coauthors, 2015: Role of mesoscale eddies in cross-frontal transport of heat and biogeochemical tracers in the Southern Ocean. *Journal of Physical Oceanography*, **45 (12)**, 3057–3081.

Eden, C., and J. Willebrand, 2001: Mechanism of interannual to decadal variability of the North Atlantic circulation. *Journal of Climate*, **14 (10)**, 2266–2280.

Ferrari, R., S. M. Griffies, A. G. Nurser, and G. K. Vallis, 2010: A boundary-value problem for the parameterized mesoscale eddy transport. *Ocean Modelling*, **32 (3-4)**, 143–156.

Fox-Kemper, B., and Coauthors, 2011: Parameterization of mixed layer eddies. III: Implementation and impact in global ocean climate simulations. *Ocean Modelling*, **39 (1-2)**, 61–78.

Fox-Kemper, B., and Coauthors, 2021: *Ocean, Cryosphere and Sea Level Change*, Vol. Climate Change 2021: The Physical Science Basis. Contribution of Working Group I to the Sixth Assessment Report of the Intergovernmental Panel on Climate Change. Cambridge University Press.

Frajka-Williams, E., B. Moat, D. Smeed, D. Rayner, W. Johns, M. Baringer, D. Volkov, and J. Collins, 2021: Atlantic meridional overturning circulation observed by the RAPID-MOCHA-WBTS (RAPID-Meridional Overturning Circulation and Heatflux Array-Western Boundary Time Series) array at 26N from 2004 to 2020 (v2020.1). NERC EDS British Oceanographic Data Centre NOC, https://doi.org/10.5285/cc1e34b3-3385-662b-e053-6c86abc03444.

Frankcombe, L. M., A. Von Der Heydt, and H. A. Dijkstra, 2010: North Atlantic multidecadal climate variability: An investigation of dominant time scales and processes. *Journal of climate*, **23 (13)**, 3626–3638.





Accepted for publication in *Journal of Climate*. DOI 10.1175/JCLI-D-22-0561.1.

Gent, P. R., J. Willebrand, T. J. McDougall, and J. C. McWilliams, 1995: Parameterizing eddy-induced tracer transports in ocean circulation models. *Journal of Physical Oceanography*, **25 (4)**, 463–474.

Getzlaff, J., C. W. Böning, C. Eden, and A. Biastoch, 2005: Signal propagation related to the North Atlantic overturning. *Geophysical research letters*, **32 (9)**.

Griffies, S. M., and Coauthors, 2015: Impacts on Ocean Heat from Transient Mesoscale Eddies in a Hierarchy of Climate Models. *Journal of Climate*, **28 (3)**, 952–977.

Hallberg, R., 2013: Using a resolution function to regulate parameterizations of oceanic mesoscale eddy effects. *Ocean Modelling*, **72**, 92–103.

Hartmann, D. L., 2015: *Global physical climatology*, Vol. 103. Newnes.

Haskins, R. K., K. I. Oliver, L. C. Jackson, S. S. Drijfhout, and R. A. Wood, 2019: Explaining asymmetry between weakening and recovery of the AMOC in a coupled climate model. *Climate dynamics*, **53 (1)**, 67–79.

Hirschi, J., and Coauthors, 2020: The Atlantic Meridional Overturning Circulation in High-Resolution Models. *Journal of Geophysical Research: Oceans*, **125 (4)**, e2019JC015 522.

Holliday, N. P., and Coauthors, 2020: Ocean circulation causes the largest freshening event for 120 years in eastern subpolar North Atlantic. *Nature communications*, **11 (1)**, 1–15.

Jackson, L., 2013: Shutdown and recovery of the AMOC in a coupled global climate model: the role of the advective feedback. *Geophysical Research Letters*, **40 (6)**, 1182–1188.

Jackson, L. C., R. Kahana, T. Graham, M. A. Ringer, T. Woollings, J. V. Mecking, and R. A. Wood, 2015: Global and European climate impacts of a slowdown of the AMOC in a high resolution GCM. *Climate Dynamics*, **45**, 3299–3316, https://doi.org/10.1007/s00382-015-2540-2, URL https://doi.org/10.1007/s00382-015-2540-2.

Jackson, L. C., and R. A. Wood, 2018: Timescales of AMOC decline in response to fresh water forcing. *Climate Dynamics*, **51 (4)**, 1333–1350.

Jackson, L. C., and Coauthors, 2020: Impact of ocean resolution and mean state on the rate of AMOC weakening. *Climate Dynamics*, **55 (7)**, 1711–1732.





Accepted for publication in *Journal of Climate*. DOI 10.1175/JCLI-D-22-0561.1.

Jansen, M. F., and L.-P. Nadeau, 2019: A Toy Model for the Response of the Residual Overturning Circulation to Surface Warming. *Journal of Physical Oceanography*, **49 (5)**, 1249–1268.

Johnson, H. L., P. Cessi, D. P. Marshall, F. Schloesser, and M. A. Spall, 2019: Recent contributions of theory to our understanding of the Atlantic Meridional Overturning Circulation. *Journal of Geophysical Research: Oceans*, **124 (8)**, 5376–5399.

Levang, S. J., and R. W. Schmitt, 2020: What Causes the AMOC to Weaken in CMIP5? *Journal of Climate*, **33 (4)**, 1535–1545.

Li, F., M. S. Lozier, G. Danabasoglu, N. P. Holliday, Y.-O. Kwon, A. Romanou, S. G. Yeager, and R. Zhang, 2019: Local and downstream relationships between Labrador Sea Water volume and North Atlantic meridional overturning circulation variability. *Journal of Climate*, **32 (13)**, 3883–3898.

Lobelle, D., C. Beaulieu, V. Livina, F. Sévellec, and E. Frajka-Williams, 2020: Detectability of an AMOC Decline in Current and Projected Climate Changes. *Geophysical Research Letters*, **47 (20)**, e2020GL089 974, https://doi.org/https://doi.org/10.1029/2020GL089974, URL https://agupubs.onlinelibrary.wiley.com/doi/abs/10.1029/2020GL089974, e2020GL089974 10.1029/2020GL089974, https://agupubs.onlinelibrary.wiley.com/doi/pdf/10.1029/2020GL089974.

Locarnini, M., and Coauthors, 2018: World ocean atlas 2018, volume 1: Temperature.

Lockwood, J. W., C. O. Dufour, S. M. Griffies, and M. Winton, 2021: On the role of the Antarctic Slope Front on the occurrence of the Weddell Sea polynya under climate change. *Journal of Climate*, 1–56.

Lozier, M., and Coauthors, 2019: A sea change in our view of overturning in the subpolar North Atlantic. *Science*, **363 (6426)**, 516–521.

Lozier, M. S., 1997: Evidence for large-scale eddy-driven gyres in the north atlantic. *Science*, **277**, 361 LP – 364, https://doi.org/10.1126/science.277.5324.361, URL http://science.sciencemag.org/content/277/5324/361.abstract.





Accepted for publication in *Journal of Climate*. DOI 10.1175/JCLI-D-22-0561.1.

Lozier, M. S., and Coauthors, 2017: Overturning in the Subpolar North Atlantic Program: A new international ocean observing system. *Bulletin of the American Meteorological Society*, **98 (4)**, 737–752.

MacGilchrist, G. A., H. L. Johnson, C. Lique, and D. P. Marshall, 2021: Demons in the North Atlantic: Variability of deep ocean ventilation. *Geophysical Research Letters*, **48 (9)**, e2020GL092 340.

McCarthy, G., and Coauthors, 2012: Observed interannual variability of the Atlantic meridional overturning circulation at 26.5°N. *Geophysical Research Letters*, **39 (19)**, https://doi.org/https://doi.org/10.1029/2012GL052933, URL https://agupubs.onlinelibrary.wiley.com/doi/abs/10.1029/2012GL052933, https://agupubs.onlinelibrary.wiley.com/doi/pdf/10.1029/2012GL052933.

McIntosh, P. C., and T. J. McDougall, 1996: Isopycnal averaging and the residual mean circulation. *Journal of Physical Oceanography*, **26 (8)**, 1655–1660.

Moat, B., and Coauthors, 2020a: Atlantic meridional overturning circulation observed by the RAPID-MOCHA-WBTS (RAPID-Meridional overturning circulation and heatflux array-Western boundary time series) array at 26N from 2004 to 2018 (v2018.2). *British Oceanographic Data Centre, National Oceanography Centre, NERC, UK*, https://doi.org/10/d3z4.

Moat, B. I., and Coauthors, 2020b: Pending recovery in the strength of the meridional overturning circulation at 26° N. *Ocean Science*, **16 (4)**, 863–874.

Pachauri, R. K., and Coauthors, 2014: *Climate change 2014: synthesis report. Contribution of Working Groups I, II and III to the fifth assessment report of the Intergovernmental Panel on Climate Change*. Ipcc.

Parker, A., and C. Ollier, 2016: There is no real evidence for a diminishing trend of the Atlantic meridional overturning circulation. *Journal of Ocean Engineering and Science*, **1 (1)**, 30–35.

Read, J., 2000: CONVEX-91: water masses and circulation of the Northeast Atlantic subpolar gyre. *Progress in Oceanography*, **48 (4)**, 461–510.





Accepted for publication in *Journal of Climate*. DOI 10.1175/JCLI-D-22-0561.1.

Rhein, M., and Coauthors, 2013: Observations: Ocean in Climate Change 2013 The Physical Science Basis in Working Group I Contribution to the Fifth Assessment Report of the Intergovernmental Panel on Climate Change (eds Stocker, TF et al.) 255–316. Cambridge University Press.

Rieck, J. K., C. W. Böning, and K. Getzlaff, 2019: The nature of eddy kinetic energy in the Labrador Sea: Different types of mesoscale eddies, their temporal variability, and impact on deep convection. *Journal of Physical Oceanography*, **49 (8)**, 2075–2094.

Roberts, C. D., L. Jackson, and D. McNeall, 2014: Is the 2004–2012 reduction of the Atlantic meridional overturning circulation significant? *Geophysical Research Letters*, **41 (9)**, 3204–3210, https://doi.org/https://doi.org/10.1002/2014GL059473, URL https://agupubs.onlinelibrary.wiley.com/doi/abs/10.1002/2014GL059473, https://agupubs.onlinelibrary.wiley.com/doi/pdf/10.1002/2014GL059473.

Roberts, M. J., and Coauthors, 2020: Sensitivity of the Atlantic meridional overturning circulation to model resolution in CMIP6 HighResMIP simulations and implications for future changes. *Journal of Advances in Modeling Earth Systems*, **12 (8)**, e2019MS002 014.

Schlitzer, R., 2000: eWOCE-Electronic Atlas of WOCE Data. *WOCE Global Data, Version 2.0 CD-ROM, WOCE Intern. Project Office, WOCE Report No. 171/00, Southampton, UK*.

Smeed, D., G. McCarthy, D. Rayner, B. Moat, W. Johns, M. Baringer, and C. Meinen, 2015: Atlantic meridional overturning circulation observed by the RAPID-MOCHA-WBTS (RAPID-Meridional overturning circulation and heatflux array-Western boundary time series) array at 26N from 2004 to 2014.

Smeed, D., and Coauthors, 2018: The North Atlantic Ocean is in a state of reduced overturning. *Geophysical Research Letters*, **45 (3)**, 1527–1533.

Smeed, D. A., and Coauthors, 2014: Observed decline of the Atlantic meridional overturning circulation 2004–2012. *Ocean Science*, **10 (1)**, 29–38.

Tagklis, F., A. Bracco, T. Ito, and R. Castelao, 2020: Submesoscale modulation of deep water formation in the Labrador Sea. *Scientific reports*, **10 (1)**, 1–13.





Accepted for publication in *Journal of Climate*. DOI 10.1175/JCLI-D-22-0561.1.

Talandier, C., 2015: La dynamique du courant profond de bord ouest dans l'Atlantique Nord et son influence sur la circulation méridienne moyenne. Ph.D. thesis, Université de Bretagne occidentale - Brest.

Talandier, C., and Coauthors, 2014: Improvements of simulated Western North Atlantic current system and impacts on the AMOC. *Ocean Modelling*, **76**, 1–19.

Waldman, R., J. Hirschi, A. Voldoire, C. Cassou, and R. Msadek, 2020: Clarifying the relation between AMOC and thermal wind: application to the centennial variability in a coupled climate model. *Journal of Physical Oceanography*, 1–61.

Weijer, W., W. Cheng, O. A. Garuba, A. Hu, and B. Nadiga, 2020: CMIP6 models predict significant 21st century decline of the Atlantic Meridional Overturning Circulation. *Geophysical Research Letters*, **47 (12)**, e2019GL086 075.

Weijer, W., M. Maltrud, M. Hecht, H. Dijkstra, and M. Kliphuis, 2012: Response of the Atlantic Ocean circulation to Greenland Ice Sheet melting in a strongly-eddying ocean model. *Geophysical Research Letters*, **39 (9)**.

Winton, M., W. G. Anderson, T. L. Delworth, S. M. Griffies, W. J. Hurlin, and A. Rosati, 2014: Has coarse ocean resolution biased simulations of transient climate sensitivity? *Geophysical research letters*, **41 (23)**, 8522–8529.

Zhang, R., 2010: Latitudinal dependence of Atlantic meridional overturning circulation (AMOC) variations. *Geophysical Research Letters*, **37 (16)**.

Zhang, R., T. L. Delworth, A. Rosati, W. G. Anderson, K. W. Dixon, H.-C. Lee, and F. Zeng, 2011: Sensitivity of the North Atlantic Ocean circulation to an abrupt change in the Nordic Sea overflow in a high resolution global coupled climate model. *Journal of Geophysical Research: Oceans*, **116 (C12)**.

Zhang, R., R. Sutton, G. Danabasoglu, Y.-O. Kwon, R. Marsh, S. G. Yeager, D. E. Amrhein, and C. M. Little, 2019: A Review of the Role of the Atlantic Meridional Overturning Circulation in Atlantic Multidecadal Variability and Associated Climate Impacts. *Reviews of Geophysics*, **57 (2)**, 316–375, https://doi.org/https://doi.org/10.1029/2019RG000644, URL https://agupubs.





Accepted for publication in *Journal of Climate*. DOI 10.1175/JCLI-D-22-0561.1.

onlinelibrary.wiley.com/doi/abs/10.1029/2019RG000644, https://agupubs.onlinelibrary.wiley.com/doi/pdf/10.1029/2019RG000644.

Zou, S., and M. S. Lozier, 2016: Breaking the linkage between Labrador Sea Water production and its advective export to the subtropical gyre. *Journal of Physical Oceanography*, **46 (7)**, 2169–2182.

Zou, S., M. S. Lozier, and M. Buckley, 2019: How is meridional coherence maintained in the lower limb of the Atlantic meridional overturning circulation? *Geophysical Research Letters*, **46 (1)**, 244–252.





Accepted for publication in *Journal of Climate*. DOI 10.1175/JCLI-D-22-0561.1.